Evolution of thermally pulsing asymptotic giant branch stars – III. Dust production at supersolar metallicities[*]

Ambra Nanni,[1]† Alessandro Bressan,[1] Paola Marigo[2] and Léo Girardi[3]

[1]*SISSA, via Bonomea 265, I-34136 Trieste, Italy*
[2]*Dipartimento di Fisica e Astronomia Galileo Galilei, Università di Padova, Vicolo dell'Osservatorio 3, I-35122 Padova, Italy*
[3]*Osservatorio Astronomico di Padova, Vicolo dell'Osservatorio 5, I-35122 Padova, Italy*

ABSTRACT

We extend the formalism presented in our recent calculations of dust ejecta from the Thermally Pulsing Asymptotic Giant Branch (TP-AGB) phase to the case of super-solar metallicity stars. The TP-AGB evolutionary models are computed with the COLIBRI code. We adopt our preferred scheme for dust growth. For M-giants, we neglect chemisputtering by H_2 molecules and for C-stars we assume a homogeneous growth scheme which is primarily controlled by the carbon over oxygen excess. At super-solar metallicities, dust forms more efficiently and silicates tend to condense significantly closer to the photosphere ($r \sim 1.5R_*$) – and thus at higher temperatures and densities – than at solar and sub-solar metallicities ($r \sim 2$–$3R_*$). In such conditions, the hypothesis of thermal decoupling between gas and dust becomes questionable, while dust heating due to collisions plays an important role. The heating mechanism delays dust condensation to slightly outer regions in the circumstellar envelope. We find that the same mechanism is not significant at solar and sub-solar metallicities. The main dust products at super-solar metallicities are silicates. We calculate the total dust ejecta and dust-to-gas ejecta, for various values of the stellar initial masses and initial metallicities $Z = 0.04, 0.06$. Merging these new calculations with those for lower metallicities it turns out that, contrary to what is often assumed, the total dust-to-gas ejecta of intermediate-mass stars exhibit only a weak dependence on the initial metal content.

Key words: stars: AGB and post-AGB – circumstellar matter – stars: mass-loss – stars: winds, outflows – dust, extinction.

1 INTRODUCTION

The production of dust during the Thermally Pulsing Asymptotic Giant Branch (TP-AGB) evolution of low- and intermediate-mass stars has been recently revisited by Zhukovska, Gail & Trieloff (2008), Ventura et al. (2012), Di Criscienzo et al. (2013) and by our group (Nanni et al. 2013), following the scheme pioneered by Gail & Sedlmayr (1999, hereafter GS99) and Ferrarotti & Gail (2006, hereafter FG06).

Making use of the TP-AGB models computed with the new COLIBRI code by Marigo et al. (2013), we have investigated the contribution to the interstellar medium (ISM) dust budget of TP-AGB stars from low metallicities ($Z = 0.001$) to the solar one ($Z = 0.02$).

At low metallicities ($Z = 0.001$), our dust ejecta, mainly of carbonaceous type, turn out to be more than one order of magnitude larger than those computed by Ventura et al. (2012) for almost all stellar initial masses. This is a direct consequence of the larger carbon excess reached by our carbon star models of low metallicities, as a cumulative result of the differences in the efficiency of the third dredge-up and hot-bottom burning, and in the duration of the TP-AGB, between our present reference version[1] of the COLIBRI TP-AGB models and those of Ventura et al. (2012).

Needless to say, a higher dust production at low metallicities could have a far-reaching relevance in the broader context of galaxy formation and evolution at high redshifts where observations of galaxies and quasars indicate that even very young objects can contain large dust reservoirs (Lilly et al. 1999; Eales et al. 2000;

---

[1] We recall that a fine calibration of the TP-AGB phase as a function of stellar mass and metallicity is currently underway so that new versions of the TP-AGB models computed with COLIBRI are also planned.

Bertoldi et al. 2003; Robson et al. 2004; Beelen et al. 2006; Dwek & Cherchneff 2011). Such large amounts of dust at early epochs, when the dust and chemical enrichment time-scales are only a fraction of a Gyr, are difficult to explain (Maiolino et al. 2004; Marchenko 2006; Dwek, Galliano & Jones 2007; Valiante et al. 2009; Michałowski, Watson & Hjorth 2010; Valiante et al. 2011; Mattsson 2011; Dwek & Cherchneff 2011; Gall, Andersen & Hjorth 2011; Pipino et al. 2011; Pipino & Matteucci 2011; Yamasawa et al. 2011; Zhukovska & Henning 2013).

Unfortunately, it is difficult to check the robustness of these predictions because, in spite of the huge literature on carbon stars at such low metallicities, there is a severe lack of *direct* observations.

At solar metallicity, direct estimates of the amount of dust produced by AGB stars and its mineralogy are provided by mid- and far-infrared observations, both in our Galaxy and in the nearby ones (Knapp 1985; Matsuura et al. 2009; Matsuura, Woods & Owen 2013). Knapp (1985) have found typical dust-to-gas ratios of $\sim 6 \times 10^{-3}$ for oxygen-rich (M) AGB stars, mainly in the form of amorphous silicates, and $\sim 10^{-3}$ for carbon-rich (C) stars, mainly as amorphous carbon. These ratios indicate that, at solar metallicity, a large fraction of the silicon must condense into dust in the circumstellar envelopes (CSEs) of these stars. The dust-to-gas ratios of M-giants predicted by Nanni et al. (2013) are within the observed range, but there is a well-known problem in reproducing their terminal velocities (Woitke 2006; Höfner 2009; Bladh et al. 2013). We have shown that, in order to reproduce the relation between terminal velocities and mass-loss rates observed in Galactic oxygen-rich giants, one may relax the strong constraint on the condensation temperature of silicates imposed by the chemisputtering destruction process (Nanni et al. 2013). The higher condensation temperatures obtained by Nanni et al. (2013) by neglecting this destruction process are in very good agreement with the laboratory measurements (Nagahara & Ozawa 1996; Nagahara et al. 2009).

In this paper we wish to extend our previous analysis to the case of super-metal-rich stars. In our Galaxy, only the Bulge may eventually harbour traces of such stellar populations, but these could be the major component in the nuclear regions of massive elliptical galaxies (Bertola et al. 1995). In some of the Virgo cluster early-type galaxies, the ISM contribution to the Mid-Infrared (MIR) emission is very low, and *Spitzer* spectroscopic observations have revealed the presence of a prominent 9.7 μm feature, typical of silicates (Bressan et al. 2006). Additional evidence, brought by *Spitzer* imaging between 4 and 16 μm and near-infrared data, indicates that this MIR emission is stellar in origin, confirming that it comes from the dusty envelopes around evolved AGB stars (Clemens et al. 2011). It has been suggested that this feature could be used as a powerful tool to disentangle the degeneracy between age and metallicity, an effect that challenges the census of stellar populations in passively evolving early-type galaxies (Bressan, Granato & Silva 1998). While this has been shown to be the case for a metal-poor massive star cluster in M81 (Mayya et al. 2013), in the case of early-type galaxies the results are much less robust because of the intrinsic difficulties encountered in modelling the intensity of the MIR emission at high metallicity (Clemens et al. 2009). These models are based on empirical scaling relations extrapolated from observations of AGB stars in the Magellanic Clouds and in the Galaxy, while direct calculations of the properties of dust in the CSEs, as those of Nanni et al. (2013), should be preferred.

The paper is organized as follows. In Section 2 we summarize the main characteristics of the TP-AGB tracks at super solar metallicities. The basic equations of the wind model presented in Nanni et al. (2013) are briefly summarized in Section 3. In Section 4 we discuss the equations governing the dust growth with particular focus on the determination of dust equilibrium temperature. In Section 5 we apply the method to the new models of TP-AGB of high metallicity while, in Section 6, we provide the corresponding dust and dust-to-gas ejecta for different masses. Finally, the results are discussed in Section 7.

2 THE TP-AGB MODELS

Stellar evolution from the pre-main sequence up to the first thermal pulse is calculated with the PARSEC code (Bressan et al. 2012) while the following evolution along the whole TP-AGB phase is computed with the COLIBRI code (Marigo et al. 2013). The reader should refer to those papers for all the details on stellar evolution. We only recall here that, thanks to the incorporation of the ÆSOPUS tool Marigo & Aringer (2009) in the COLIBRI code our TP-AGB evolution models are the first ever to include accurate on-the-fly computation of the equation of the equation of state for $\simeq 300$ atomic and $\simeq 500$ molecular species, as well as of the Rosseland mean gas opacities throughout the convective envelope and the atmosphere. This new advance guarantees full consistency between the envelope structure and the surface chemical abundances, and therefore robustly tracks the impact of third dredge-up mixing episodes and hot-bottom burning.

In particular, with COLIBRI we are able to follow in detail the evolution of the surface C/O ratio, which critically affects molecular chemistry, opacity and effective temperature, every time it goes across the critical values around unity (Marigo 2002; Marigo & Girardi 2007). As a consequence, the C/O ratio plays a major role in determining the chemical and physical properties of the dust. As discussed in Nanni et al. (2013), in M-stars (C/O < 1) the main dust species are amorphous silicates, quartz (SiO_2) and corundum (Al_2O_3) (Ossenkopf, Henning & Mathis 1992; Tielens et al. 1998) while, in C-stars (C/O > 1), the dust produced is predominantly amorphous carbon and silicon carbide (SiC) (Groenewegen et al. 1998). At super-solar metallicity however, the latter phase is practically absent, as can be seen from Figs 1 and 2. Only the model of $M = 5 \, M_\odot$ with $Z = 0.04$ is able to reach a C/O ratio slightly larger than unity.

The almost complete lack of the C-star phase is the combined result of the minor efficiency of the third dredge-up and the shorter lifetimes in TP-AGB models with high initial metallicity. First, the minimum stellar mass at which the third dredge-up is expected to take place increases with the metallicity, while the depth of the third dredge-up becomes progressively shallower. Secondly, even TP-AGB models that experience the third dredge-up may not be able to reach the condition C/O > 1, because mass loss by stellar winds prevents them from undergoing the number of thermal pulses necessary to bring the surface carbon abundance above the already high initial content of oxygen. We also underline the fact that at high metallicities, such those considered in this work ($Z = 0.04, 0.06$), hot bottom burning is not active in most of the more massive AGB stars, except for those with $M \simeq 6 \, M_\odot$, close to upper limit of the mass range covered by intermediate-mass stars. As a consequence, these models do not present the overluminosity effect usually associated with hot-bottom burning, and their luminosity evolution during the quiescent stages is mainly controlled by the mass of the H-exhausted core (see third-row panels in Figs 1 and 2).

We notice that the effective temperatures of these models decrease on average, as the metallicity increases, as expected as a consequence of the higher atmospheric opacity. Although the surface C/O ratio remains lower than unity during the whole TP-AGB
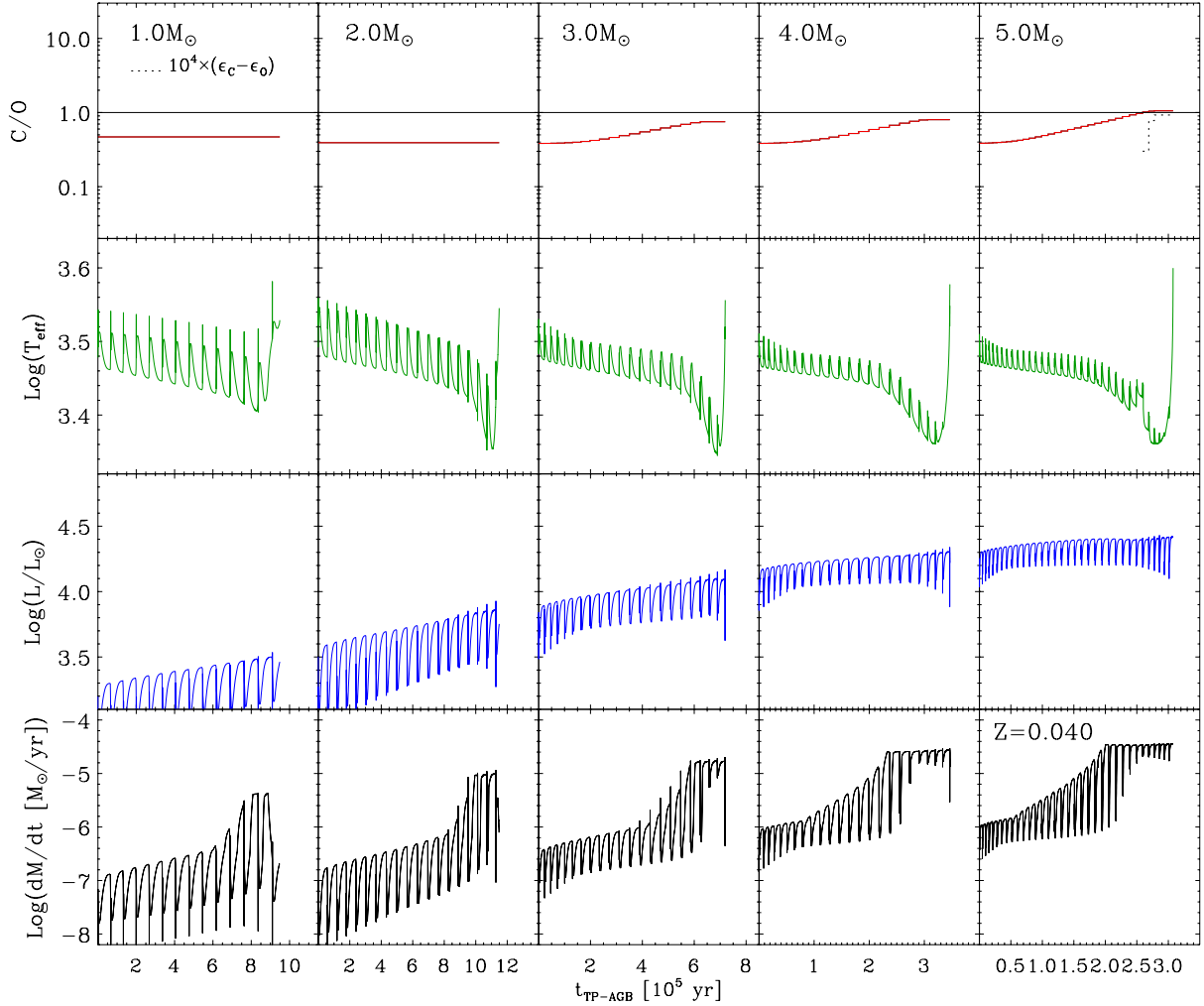
Figure 1. Evolution of surface C/O, carbon excess $\epsilon_C - \epsilon_O$ (only when positive), effective temperature, luminosity, and mass-loss rate during the whole TP-AGB phase of a few selected models with initial metallicity $Z = 0.04$, computed with the COLIBRI code (Marigo et al. 2013). These quantities are the key input stellar parameters for our dust growth model. Time is counted from the first thermal pulse. Note that effective temperature and luminosity derive from the solution of the full set of stellar structure equations across the envelope and the atmosphere, and not from analytic relations as commonly done in synthetic TP-AGB models. The value of the C/O ratio is always below unity, but for the late stages of the model with initial mass $M = 5.0\,M_\odot$. See the text for more details.

evolution, the tracks show a clear and sudden cooling during the late evolutionary stages (see second-row panels of Figs 1 and 2). This happens as soon as the TP-AGB models enter the super-wind regime and their envelope starts being dramatically reduced (yet, still not so much to leave the AGB towards higher T_{eff}). In fact, we know from theory that, at given chemical composition, the Hayashi lines shift to lower T_{eff} at decreasing stellar mass (see e.g. fig. 16 of Marigo et al. 2013).

According to our adopted scheme of mass loss (as detailed in section 6.2 of Marigo et al. 2013), because of their low effective temperatures, super-metallicity TP-AGB models quickly reach the super-wind phase, which is treated following the prescriptions of Vassiliadis & Wood (1993, their equations 1 and 3). This explains why our predicted mass-loss rates flatten out to nearly constant values, almost irrespective of both stellar mass and metallicity (see bottom panels Figs 1 and 2).

3 WIND MODEL

The adopted dusty wind model has been thoroughly described in Nanni et al. (2013).

Following FG06, the equations below describe a stationary and spherically symmetric outflow of one-fluid component, assuming that there is no drift velocity between gas and dust. Neglecting the contribution of the gas pressure gradient we have

$$v\frac{dv}{dr} = -\frac{GM_*}{r^2}(1 - \Gamma),\tag{1}$$

where

$$\Gamma = \frac{L_*}{4\pi c G M_*}\kappa\tag{2}$$

is the ratio between the radiative and the gravitational accelerations. The density profile $\rho(r)$ across the wind is determined by the continuity equation:

$$\rho(r) = \frac{\dot{M}}{4\pi r^2 v}.\tag{3}$$

The temperature structure $T(r)$ is described with the approximation for a grey and spherically symmetric extended atmosphere (Lucy 1971, 1976)

$$T(r)^4 = T_{\text{eff}}^4\left[W(r) + \frac{3}{4}\tau\right],\tag{4}$$
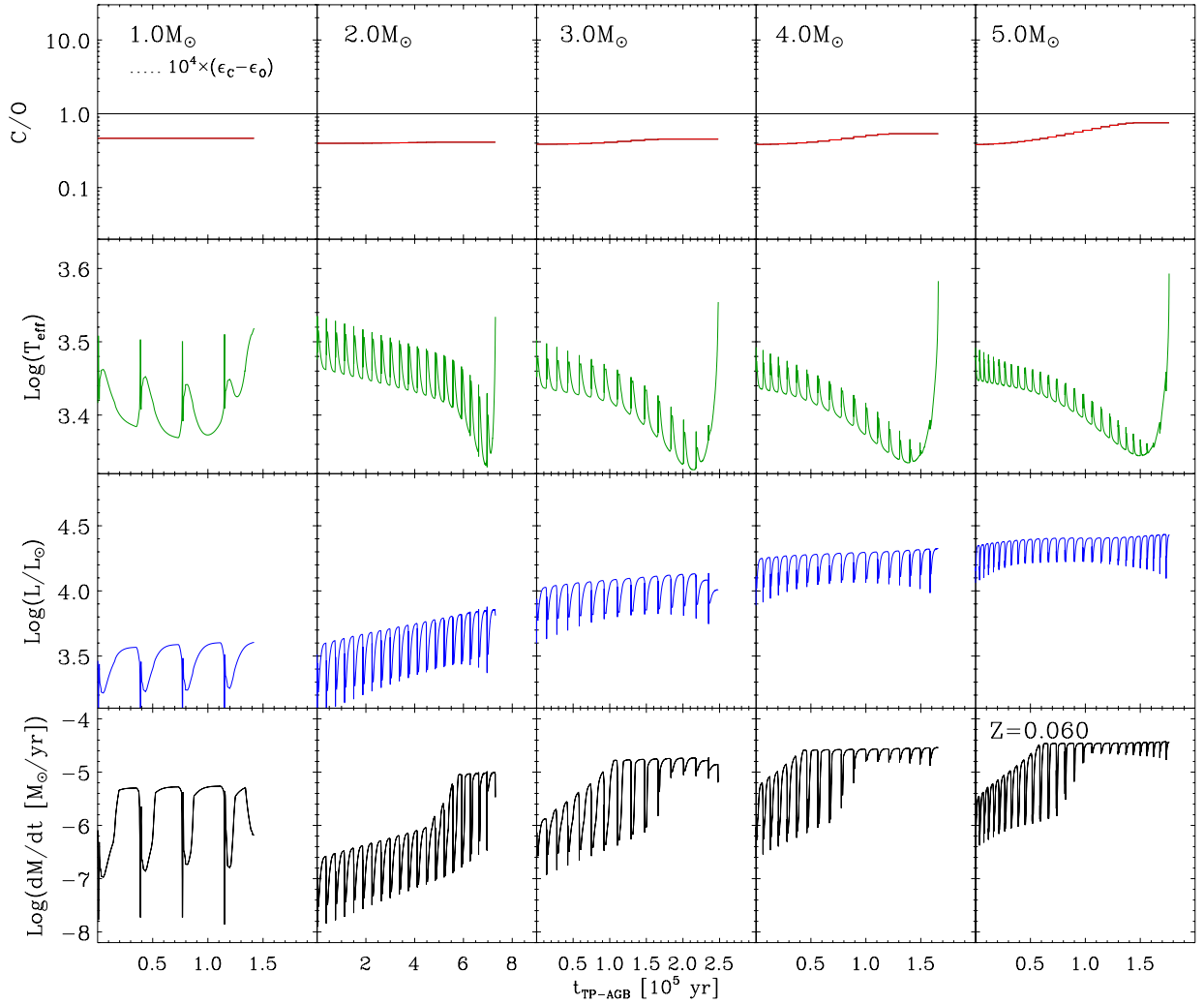
Figure 2. The same as in Fig. 1, but for initial metallicity $Z = 0.06$.

where

$$W(r) = \frac{1}{2}\left[1 - \sqrt{1 - \left(\frac{R_*}{r}\right)^2}\right] \quad (5)$$

represents the dilution factor, R_* is the photospheric radius and τ is the optical depth that obeys the differential equation

$$\frac{d\tau}{dr} = -\rho\kappa \frac{R_*^2}{r^2}, \quad (6)$$

with the boundary condition

$$\lim_{r \to \infty} \tau = 0. \quad (7)$$

The opacity κ is given by the sum of the gas contribution and of all the dust species

$$\kappa = \kappa_{\text{gas}} + \sum_i f_i \kappa_i \quad [\text{cm}^2 \text{ g}^{-1}] \quad (8)$$

where $\kappa_{\text{gas}} = 10^{-8}\rho^{2/3}T^3$ (Bell & Lin 1994), f_i is the degree of condensation of the key-element[2] into a certain dust species i and

κ_i is its opacity, computed assuming the complete condensation of the key-element initially available in the gas phase. The degree of condensation is usually written as

$$f_i = n_{k,i} \frac{4\pi(a_i^3 - a_0^3)\rho_{d,i}}{3m_{d,i}\epsilon_{k,i}} \epsilon_s, \quad (9)$$

where $n_{k,i}$ is the number of atoms of the key-element present in one monomer of the dust species i; $m_{d,i}$ is the mass of the monomer; a_i denotes the grain size (radius) and a_0 is the initial grain size; $\rho_{d,i}$ is the dust density of the grain; $\epsilon_{k,i}, \epsilon_s$ are the number densities of the key-element, and of the initial number of dust grains (seed nuclei) normalized to the number density of hydrogen N_{H}, respectively. Dust opacities are computed from the optical properties of grains, as in Nanni et al. (2013). For M-stars, the (n, k) data of olivine and pyroxene are taken from Ossenkopf et al. (1992), and for corundum we refer to Begemann et al. (1997). For C-stars the (n, k) data of amorphous carbon are from Hanner (1988), while we use Pègouriè (1988) for silicon carbide. Iron opacity is derived from Leksina & Penkina (1967). Once dust is formed, its opacity increases and the contribution of the gas becomes negligible. The wind accelerates if the opacity becomes large enough so that $\Gamma > 1$.

[2] Following FG06, the key-element of a given dust species denotes the least abundant element among those involved in its formation; e.g. Si is the key-element of the silicate compounds in O-rich stars.

3.1 Accretion of dust grains

The growth of dust grains is determined by the balance between the rate of effective collisions of molecules on the grain surface, J_i^{gr}, and its decomposition rate, J_i^{dec}. The differential equation describing the dust growth is usually expressed in terms of the variation of the grain radius, a_i,

$$\frac{\mathrm{d}a_i}{\mathrm{d}t} = V_{0,i}(J_i^{\mathrm{gr}} - J_i^{\mathrm{dec}}). \tag{10}$$

The growth rate for each dust species, i, is defined as the minimum between the rates of effective collisions on the grain surface of the gas molecules involved in the formation of the dust monomer through the formation reactions. The molecular species determining such a rate is named 'rate-determining species'.

$$J_i^{\mathrm{gr}} = \min\left[s_i \frac{\alpha_i n_{j,g} v_{\mathrm{th},j}(T_{\mathrm{gas}})}{s_j} \right], \tag{11}$$

where $n_{j,g}$ is the number density of the molecule j in the gas phase, T_{gas} is the gas temperature given by equation (4), $v_{\mathrm{th},j}(T_{\mathrm{gas}})$ is the corresponding thermal velocity, s_j is its stoichiometric coefficient in the dust formation reaction, s_i is the stoichiometric coefficient of the monomer of the dust species i and α_i is its sticking coefficient.

4 DUST GROWTH

Dust formation in the expanding CSE of an AGB star can be modelled as a two-step process. Initially, small stable refractory aggregates, seed nuclei, are supposed to form from the molecules in the gas phase (nucleation process) and then, as the temperature decreases below a certain critical value identified as the dust condensation temperature T_{cond}, accretion on the seed surface occurs by addition of other molecules. Following a commonly accepted scenario, the first to form are the most refractory aggregates, and then the process proceeds by heterogeneous accretion (Gail & Sedlmayr 1986; Jeong et al. 2003). Since the details of the nucleation process are still poorly understood (Goumans & Bromley 2012) it is common practice to express the abundance of seed nuclei as a tunable parameter, ϵ_s. The abundance of seeds usually adopted for solar metallicity, $\epsilon_s = 10^{-13}$, appears to be consistent with detailed nucleation computations by Jeong et al. (2003), as well as in very good agreement with the value inferred by Knapp (1985) for a sample of Galactic M-giants. Adopting $\epsilon_s = 10^{-13}$, Nanni et al. (2013) obtained grains with typical sizes of $\sim 0.15\,\mu\mathrm{m}$, in agreement with the observations. Similar considerations and results hold also for amorphous carbon. In principle, the abundance of seeds should scale with the abundance of the key-element at varying metallicities. However, due to the uncertainties affecting the determination of the chemistry of the first refractory compounds (Jeong et al. 2003), we simply scale the seed number with the total metallicity:

$$\epsilon_{s,M} = \epsilon_s \left(\frac{Z}{Z_{\mathrm{ISM}}} \right), \tag{12}$$

where $Z_{\mathrm{ISM}} = 0.017$ is the assumed local metallicity of the ISM.

4.1 The dust condensation temperature T_{cond}

As thoroughly discussed in the literature, the dust condensation temperature, T_{cond}, is a critical parameter that affects the dust condensation radius and consequently the wind dynamics (Höfner 2008, 2009; Bladh et al. 2013).

In Nanni et al. (2013), the condensation radius is defined as the distance from the photosphere at which the condition $J_i^{\mathrm{gr}} = J_i^{\mathrm{dec}}$

is satisfied and T_{cond} is the equilibrium temperature that the dust would have at the condensation radius.

The equilibrium temperature is computed from the balance between the energy absorbed and re-emitted by the dust grains. A remarkable difference with respect to Nanni et al. (2013) is that here we have also added the heating rate due to collisions with H_2 molecules. In other works (GS99 and FG06), this term has been neglected because, at the low condensation temperatures obtained for silicates and carbon ($T_{\mathrm{gas}} \leq 1100\,\mathrm{K}$), this term turns out to be negligible. However, in Nanni et al. (2013) and in this paper as well, the condensation temperature for silicates can reach values in excess of $T_{\mathrm{dust}} \sim 1400\,\mathrm{K}$. Dust may thus form significantly closer to the photosphere ($r \sim 2$–$3R_*$) than in GS99 and FG06 ($r \sim 5$–$7R_*$), and, especially at the high metallicities considered in this paper, it is important to check whether the collisions term could be important. At this metallicities, in fact, the number density of the particles in the gas phase, and therefore J_i^{gr}, is larger than lower metallicity cases. As a consequence, dust condenses closer to the photosphere, because the condition $J_i^{\mathrm{gr}} = J_i^{\mathrm{dec}}$ is reached at smaller radii. At this radius the gas density and temperature are also larger, and dust and gas might be coupled.

Assuming that at each collision a dust grain gains an energy amount equal to $3/2 k_B(T_{\mathrm{gas}} - T_{\mathrm{dust}})$ (Lucy 1976), dust heating by gas molecules (in erg s^{-1}) can be expressed as

$$H_{\mathrm{collision}} = 4\pi a^2 3/2 k_B (T_{\mathrm{gas}} - T_{\mathrm{dust}}) N_{H_2} v_{\mathrm{th}}. \tag{13}$$

Correspondingly, the energy balance equation used by Nanni et al. (2013) for deriving the dust condensation temperature is modified as

$$\sigma\, T_{\mathrm{dust}}^4 Q_{\mathrm{abs,P}}(a, T_{\mathrm{dust}}) = \sigma\, T_{\mathrm{eff}}^4 Q_{\mathrm{abs,P}}(a, T_{\mathrm{eff}}) W(r) + \frac{H_{\mathrm{collision}}}{4\pi a^2}, \tag{14}$$

where $Q_{\mathrm{abs,P}}$ is the *Planck* averaged absorption coefficient expressed explicitly as a function of the temperature and grain size, $W(r)$ is the dilution factor defined in equation (5) and N_{H_2} is the number density of H_2 molecules that is approximately equal to $N_H/2$. As discussed in the following, we find that the heating term due to collisions becomes important at the highest mass-loss rates, when dust tends to condense close to the photosphere.

4.1.1 M-star models

For M-giants the main destruction process of dust grains is supposed to be sublimation caused by heating of the grains due to absorption of stellar radiation and by collisions with gas particles. Chemisputtering by H_2 molecules, considered to be fully efficient by GS99, is instead neglected. Therefore the decomposition rate is $J_i^{\mathrm{dec}} = J_i^{\mathrm{sub}}$. This quantity is determined by considering that it must equal the growth rate in chemical equilibrium conditions and that the rate so determined also holds outside equilibrium. We thus obtain from equation (11), after eliminating $n_{j,g}$ with the partial pressure and the temperature,

$$J_i^{\mathrm{sub}} = \alpha_i v_{\mathrm{th},j}(T_{\mathrm{dust}}) \frac{p(T_{\mathrm{dust}})}{k_B T_{\mathrm{dust}}}, \tag{15}$$

where T_{dust} is the dust equilibrium temperature determined with equation (14), $v_{\mathrm{th},j}(T_{\mathrm{dust}})$ is the thermal velocity of the molecule ejected from the grain surface and k_B is the Boltzmann constant. The quantity $p(T_{\mathrm{dust}})$ is the saturated vapour pressure at the dust

temperature that can be expressed with the Clausius–Clapeyron equation

$$\log p(T_{dust}) = -\frac{c_1}{T_{dust}} + c_2 \qquad (16)$$

where c_1 and c_2 are sublimation constants, characteristic of the species under consideration. The constant c_1 contains the latent heat of sublimation of the dust species and the constant c_2 is slightly dependent on the temperature. The quantities c_1 and c_2 may be obtained either directly from thermodynamical data (Duschl, Gail & Tscharnuter 1996), or by fitting with equation (16) the results of sublimation experiments (Kimura et al. 2002; Kobayashi et al. 2009, 2011). We notice that the sublimation rate depends on the dust equilibrium temperature T_{dust} which, in our model, can be defined only near the condensation point (Section 4.1). Thus, instead of integrating the full equation (10), we first determine the condensation point within the CSE by comparing the growth rate with the maximum sublimation rate, i.e. the sublimation rate obtained by setting $\alpha_i = 1$ in equation (15). This point is defined by the condition $J_i^{gr} = J_{i,\max}^{dec}$ and provides also the condensation temperature. Beyond this point, we assume that the sublimation rate is negligible in the right-hand side of equation (10). In this way, the condensation temperature depends both on the dust species which determines $J_{i,\max}^{dec}$ and on the physical conditions of the CSE, which determine J_i^{gr}. Since the real sublimation rate is only α_i times the maximum sublimation rate, the above condition implies that condensation begins when the growth rate is $\sim 1/\alpha_i$ (~ 10 for silicates) the real sublimation rate. The corresponding super-saturation ratio is also $\sim 1/\alpha_i$. Therefore, differently from other models found in the literature, silicate condensation temperature is not assumed a priori, but is derived as previously described. We notice that our choice of retaining only the growth term in equation (10) does not affect the accuracy of the results, since, beyond the condensation point, the sublimation rate decreases almost exponentially with the temperature.

4.1.2 C-star models

For amorphous carbon, we consider the homogeneous accretion that initially proceeds through complex reactions of C_2H_2 addition, forming isolated chains that subsequently coalesce into larger cores. Further growth of carbon mantles on these initial seeds can continue through vapour condensation (GS99). According to Cherchneff, Barker & Tielens (1992), the chain of C_2H_2 addition reactions have a bottleneck in the formation of the benzene because it becomes effective only when the *gas* temperature is below $T_{gas} = 1100$ K. Therefore, while the sublimation temperature of solid carbon can exceed ~ 1600 K, its growth should be inhibited above $T_{gas} = 1100$ K. Thus, following FG06, we do not consider any destruction reaction in the case of amorphous carbon, but we assume that it can grow only when $T_{gas} \leq 1100$ K.

4.2 Method of solution and initial conditions

The system of differential equations describing the dust evolution is given by equations (1), (6) and an equation like (10) for each dust species. In M-stars we consider the evolution of corundum (Al_2O_3), quartz (SiO_2), iron, olivine ($Mg_{2x}Fe_{2(1-x)}SiO_4$) and pyroxene ($Mg_xFe_{1-x}SiO_3$). The quantity x is the fractional abundance of Mg molecules with respect to the sum of Mg and Fe molecules and it ranges from 0 to 1. In C-stars we consider amorphous carbon, silicon carbide (SiC) and iron. The independent variable of the system is the radial distance r, whereas the dependent variables are the

velocity, v, the optical depth, τ, the grain size for each dust species, a_i and x. The quantities that determine the wind structure are the gas temperature and density profiles, $T(r)$ and $\rho(r)$, the total opacity, κ, the dust condensation fraction, f, and Γ.

Since the boundary condition on τ (equation 7) is at infinity, but all the other conditions are at the condensation radius, we solve the system by means of the shooting method thoroughly described in Nanni et al. (2013). The reactions assumed for dust formation are taken from Gail & Sedlmayr (1998), for corundum, and FG06 for all the other dust compounds. The thermodynamical data for the decomposition rates are taken from Sharp & Huebner (1990) with the exception of $FeSiO_3$ and SiC for which we use the data taken by Barin & Platzki (1995). The values of the sticking coefficients are taken from laboratory measurements, when available, or from theoretical computations. For olivine we adopt $\alpha_{ol} \sim 0.2$ determined from evaporation experiments of forsterite by Nanni et al. (2013). For iron and quartz the experimental values are $\alpha_{Fe} \sim 1$ and $\alpha_{qu} \sim 0.01$, respectively (Landolt-Börnstein 1968). For the growth of SiC a value of $\alpha_{SiC} \sim 1$ has been determined by Råback (1999). For pyroxene we adopt the same value as that used for olivine. For corundum we chose the maximum possible value, i.e. $\alpha_{co} = 1$. Finally, for amorphous carbon the usual assumption is to adopt $\alpha_C = 1$. The effects of adopting a lower value for carbon sticking coefficient have been discussed in Nanni et al. (2013).

For the computation of the opacities we use a flat dust size distribution ($x_g = 0.1$) from $a_{min} = 0.005$ μm to $a_{max} = 0.18$ μm. This choice is consistent with the grain size distribution obtained from the integration. The number of initial seeds is set to $\epsilon_s = 10^{-13}$ and their initial size is assumed to be $a_0 = 0.001$ μm (FG06). The value of initial velocity of the outflow was arbitrarily chosen to be 0.5 km s^{-1}. If Γ never exceeds the unity, dust is not able to drive the wind – inefficient dust-driven case according to FG06 and Höfner (2009) – and we neglect the fraction of dust condensed in these phases. This approximation does not affect the ejecta of the major dust species because the mass-loss rates corresponding to inefficient dust-driven wind cases are low. We also exclude from the calculations the models with mass-loss rates below 10^{-8} M$_\odot$ yr^{-1} since in these cases, dust formation is negligible (FG06).

5 RESULTS

We follow dust growth in the CSEs of a few selected evolutionary TP-AGB tracks, extracted from the set of Marigo et al. (2013). The differences that arise in the CSEs structure as a consequence of including or neglecting the collisional heating term, equation (13), in equation (14), are shown in Fig. 3 for $Z = 0.02$ and in Fig. 4 for $Z = 0.06$, respectively. In the case of $Z = 0.02$ we select two cases, one with an intermediate mass-loss rate ($\sim 10^{-6}$ M$_\odot$ yr^{-1}) and the other with a high mass-loss rate ($\sim 10^{-5}$ M$_\odot$ yr^{-1}). In the panels of Fig. 3, we plot the run of the gas and dust temperature, the condensation fraction of silicates, the expansion velocity and the density, as a function of the radius within the CSE. The upper panels show the case in which the collisional heating term is neglected while in the lower ones, we include this contribution to the energy balance equation. When the heating term is included, the dust equilibrium temperature at a given radius rises, the sublimation rate increases (equation 15) and, as a consequence, the condensation point shifts outwards, where this heating term becomes less important. As shown in the left-hand panel of Fig. 3, the structure of the CSE remains practically unchanged for a mass-loss rate of $\dot{M} \sim 10^{-6}$ M$_\odot$ yr^{-1}. When the heating term is included in the cases representative of a large mass-loss rate, $\dot{M} \sim 10^{-5}$ M$_\odot$ yr^{-1},
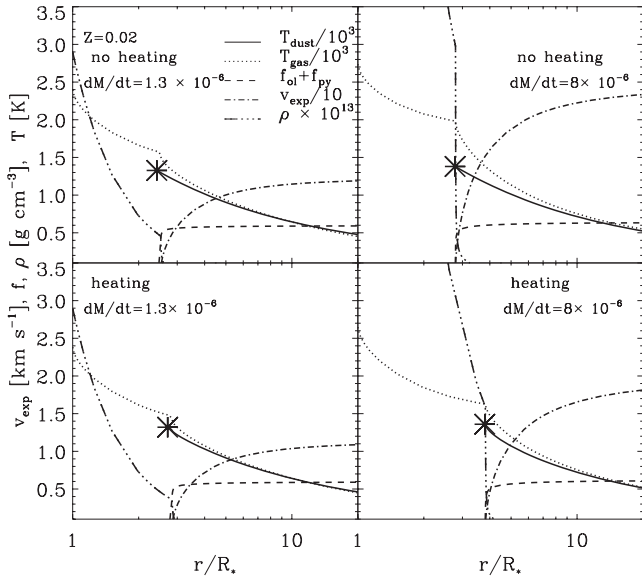
Figure 3. Effects of including the collisional heating term in the energy balance equation (equation 14), in the structure of the CSE. We show a model with initial mass $M = 1.5\,M_\odot$ and metallicity $Z = 0.02$, and for intermediate (left panels) and high (right panels) mass-loss rates as indicated, respectively. In the upper panels the heating term is neglected, as in Nanni et al. (2013) while, in the lower panels, the term is included. In each panel we show the dust equilibrium temperature (solid line), the gas temperature (dotted line), the condensation fraction of silicates (dashed line), the expansion velocity (dot–dashed line) and the gas density (triple-dot–dashed line). The asterisk marks the condensation temperature.
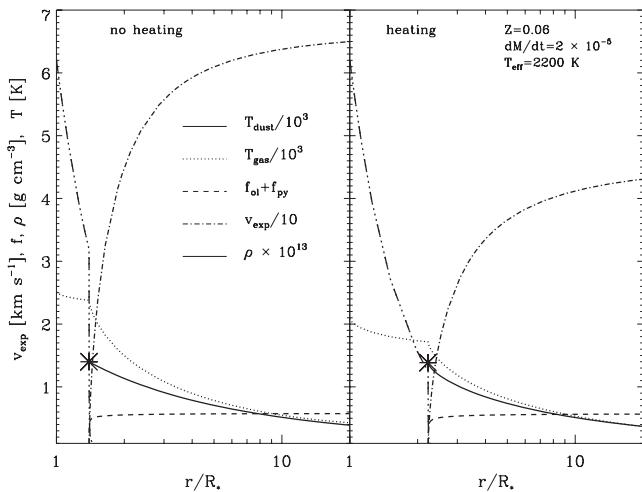

Figure 4. As in Fig. 3, but for a model of initial mass $M = 4\,M_\odot$, metallicity $Z = 0.06$ and high mass-loss rate. In the left panel, the heating term is neglected while, in the right panel, the term is included. Notice that, at this high metallicity, neglecting the heating term leads to inconsistent results. See text for more details

the condensation radius increases by about 50 per cent and the expansion velocity decreases by 20 per cent. The final condensation fraction remains almost unchanged. Finally, we notice that this term does not affect significantly the dust condensation temperature, which we obtain through the energy balance, but only the radius at which this condensation temperature is reached. An overall com-
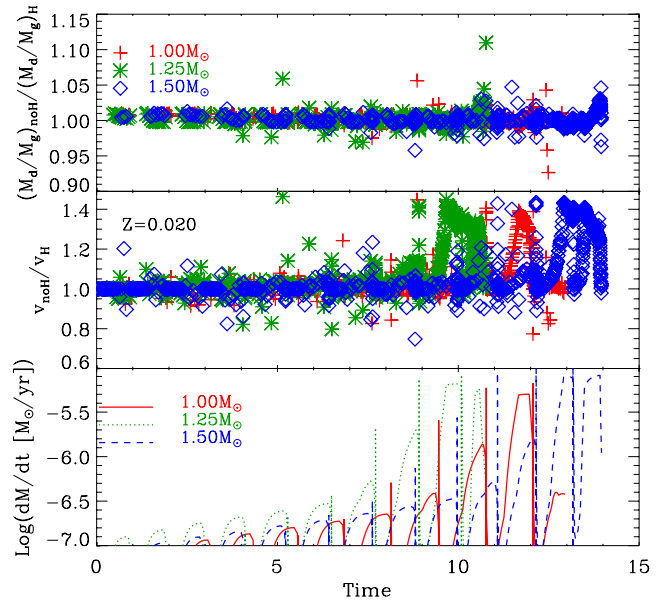

Figure 5. Upper panel: comparison of dust-to-gas ratios obtained by neglecting or considering the heating term of equation (14). We show their ratios for the cases with $M = 1, 1.25, 1.5\,M_\odot$ and metallicity $Z = 0.02$. Middle panel: the same as in the upper panel but for the expansion velocities. Lower panel: mass-loss rate as a function of time. This quantity does not depend on the specific model assumption, but is characteristic of the TP-AGB phase considered.

parison of the differences in the dust-to-gas ratios and expansion velocities between the no-heating and heating models is shown in Fig. 5 for $M = 1, 1.25, 1.5\,M_\odot$ yr^{-1} at $Z = 0.02$. We first notice that the variation of these two quantities in the two schemes is modulated by the mass-loss rate that is independent of the scheme adopted. The difference between the heating and no-heating cases is within 5 per cent for the dust-to-gas ratios, while for the expansion velocities, the differences are up to 40 per cent at the highest mass-loss rates. However, on average, the effects of neglecting the heating term are small. In particular, the differences between the dust ejecta are almost negligible.

At super-solar metallicity, $Z = 0.06$, we should consider that (i) the gas is characterized by a higher number density of metals and, (ii) the effective temperatures of the models are generally lower than in the solar metallicity case. If the collisional heating term is neglected, both circumstances allow dust to cool down efficiently even at small distances from the photosphere, $r \sim 1.5R_*$. Here the density and the temperature are higher than in the more external regions, giving rise to larger optical depths at the condensation point. In the case computed without the collisional heating term, shown in the left panel of Fig. 4, the solution requires an optical depth at the condensation point that is larger than unity, which is inconsistent with the adopted grey atmosphere temperature structure (i.e. the gas temperature below the condensation point is even larger than the effective temperature). Thus, solving the system of equations without the heating term at high mass-loss rates for the high-metallicity case, $Z = 0.06$, leads to inconsistent results. The importance of the collisional heating term can be appreciated by looking at the right panel of Fig. 4. This term prevents dust from condensing too early in the envelope and, setting a natural threshold to the condensation radius, prevents the occurrence of inconsistent solutions.
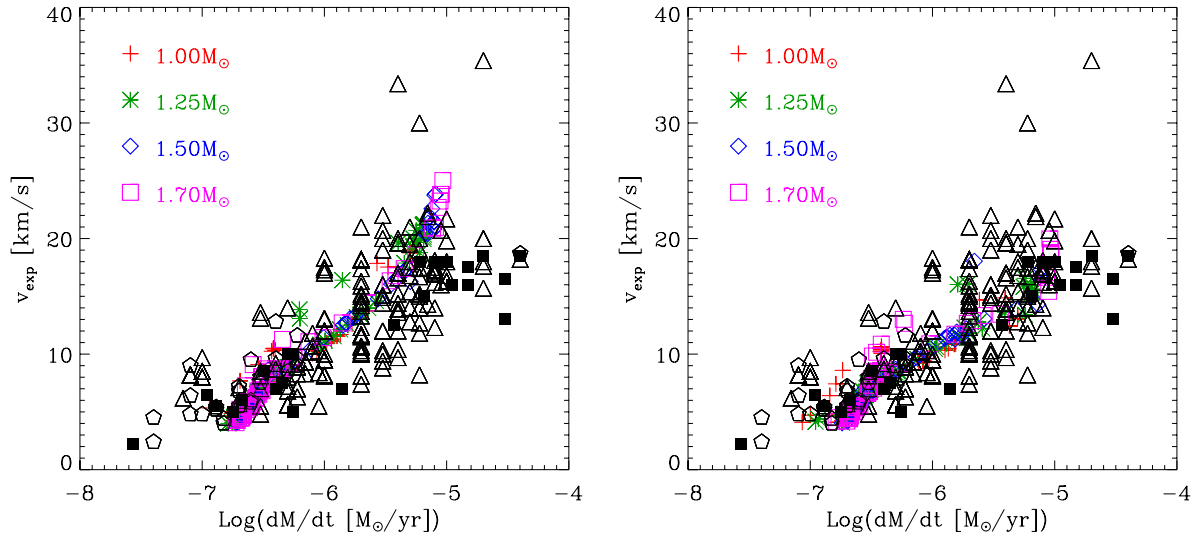
Figure 6. Expansion velocities of circumstellar outflows against mass-loss rates of variable M-stars. Observations of Galactic M-stars by Loup et al. ([1993]) (black triangles), González Delgado et al. ([2003]) (black pentagons) and Schöier et al. ([2013]) (black squares) are compared with predicted expansion velocities for a few selected TP-AGB tracks with $Z = 0.02$ for the values of initial stellar masses listed in upper left of each figure. Left panel: comparison with simulations that do not include the heating effect due to H_2 collisions. Right panel: comparison with models that include the effect of the heating. For this metallicity the results do not change significantly.

5.1 Expansion velocities

In addition to Fig. 5, we show in Fig. 6 the expansion velocities of TP-AGB stars with masses $M = 1, 1.25, 1.5, 1.7 \, M_\odot$ and $Z = 0.02$, taken from Nanni et al. ([2013]) as shown in Table 1, against the corresponding mass-loss rates both for the no-heating (left panel) and the heating (right panel) scenarios. For each track we plot a discrete number of points, selected from a randomly generated uniform distribution of ages that samples the entire TP-AGB phase of each star. This selection method better represents the expected expansion velocity distribution. The models are compared with the velocities observed in Galactic M-type AGB stars. Data of mass-loss rates and expansion velocities are taken from Loup et al. ([1993]) (black triangles), González Delgado et al. ([2003]) (black pentagons) and Schöier et al. ([2013]) (black squares). Data from Loup et al. ([1993]) and Schöier et al. ([2013]) are derived from observations of ^{12}CO and HCN rotational transitions, whereas González Delgado et al. ([2003]) obtained their values from the interpretation of SiO rotational transition lines. Following the above authors, the uncertainties of the velocity measurements are small, typically ≤10 per cent, while those of the mass-loss rates can be significantly higher reaching, in some cases, even an order of magnitude. For the metallicity we have

adopted $Z = 0.02$, which is the value derived by Smith & Lambert ([1985]) and Lambert et al. ([1986]) for their sample of Galactic M and C giants. The stellar masses are not observationally determined and we assume that they are mostly below $M \lesssim 2 \, M_\odot$ because M-giants of higher masses are more rare in our Galaxy.

From the inspection of the models and of Fig. 6 we see first that, at solar metallicity, neglecting the heating term does never lead to inconsistent models. Secondly, we see that the effects of collisions become important only at the highest mass-loss rates, where they produce a decrease of the expansion velocities of about 10–20 per cent. Thus, at solar metallicity, collisional heating is of minor importance, with respect to other uncertainties. At the lower metallicities the effect is even less important.

At super-solar metallicities, the combined effects of higher opacities and lower effective temperatures favour dust condensation very close to the stellar photosphere and the collisional heating term in equation (14) is no more negligible. Furthermore, at supersolar metallicity, only the model of $M = 5 \, M_\odot$ with $Z = 0.04$ is able to reach a C/O ratio larger than unity, as shown in Figs 1 and 2. As a consequence the C-star phase is practically absent and we will focus the discussion on the M-giant stars.

Table 1. Dust ejecta at $Z = 0.04$ and $Z = 0.06$.

| Z		0.04					0.06				
M_i [M$_\odot$]	Age log (yr)	Sil	Fe	Al$_2$O$_3$ log (M/M$_\odot$)	C	SiC	Age log (yr)	Sil	Fe	Al$_2$O$_3$ log (M/M$_\odot$)	C	SiC
1.00	10.136	−2.59	−6.41	−4.21	–	–	10.095	−2.46	−7.08	−4.82	–	–
1.25	9.793	−2.39	−6.43	−4.13	–	–	9.765	−2.25	−6.87	−4.62	–	–
1.50	9.551	−2.27	−6.26	−4.03	–	–	9.528	−2.11	−6.69	−4.05	–	–
1.70	9.392	−2.18	−5.96	−3.94	–	–	9.372	−2.07	−6.74	−3.87	–	–
2.00	9.226	−2.09	−6.20	−3.84	–	–	9.188	−1.96	−6.63	−3.71	–	–
3.00	8.697	−1.92	−6.40	−3.75	–	–	8.647	−1.71	−6.36	−3.89	–	–
4.00	8.323	−1.81	−6.05	−3.77	–	–	8.273	−1.58	−6.23	−4.06	–	–
5.00	8.057	−2.17	−2.67	−3.72	−6.06	−2.77	8.001	−1.50	−6.09	−3.82	–	–
6.00	7.852	−1.55	−6.11	−4.18	–	–	7.794	−1.41	−6.00	−4.99	–	–
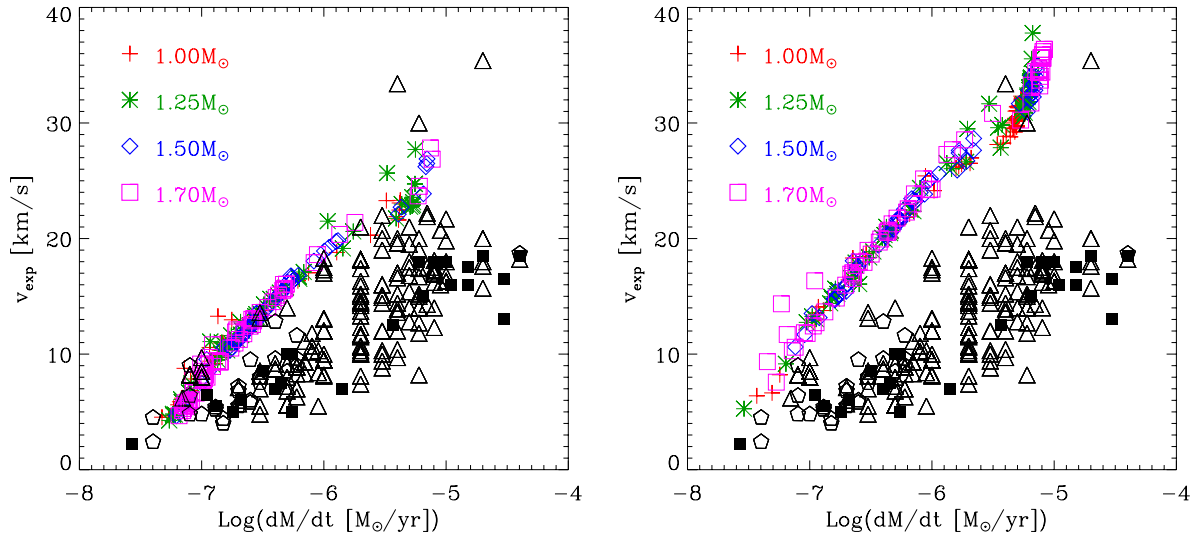
Figure 7. The same as the right panel of Fig. 6 for $Z = 0.04$ (left panel) and $Z = 0.06$ (right panel).

The expansion velocities of our super-metal-rich models are plotted against the mass-loss rates in Fig. 7. We used the same method adopted in Fig. 6 and we also put the Galactic data only to check where high-metallicity stars are expected in this plot with respect to the ones at solar metallicity. At increasing metallicity the velocity at a given mass-loss rate is higher because of the larger gas opacity. We notice that the velocities of the most metal-rich models, $Z = 0.06$, are definitely larger than the observed velocities. However a few observed M-type AGB stars, along the highest envelope of the data, could be compatible with low-mass super-metal-rich stars with $Z \sim 0.04$.

5.2 Condensation fractions, composition, dust sizes and dust mass-loss rates

As already mentioned, super-metal-rich stars are dominated by silicate dust production, i.e. olivine and pyroxene. This is shown in Figs 8 and 9, for $Z = 0.04$ and $Z = 0.06$. In the same figures, the sizes of dust grains are shown. The typical value reached is between $a = 0.1$ μm and $a = 0.15$ μm, for all the stellar masses and metallicities. These values are similar to those of the solar metallicity case and we confirm that, because of our assumptions, the maximum value of the size remains almost independent of the metallicity of the star, even up to the most metal-rich case considered here. The reason is that in our model both the initial number of seeds and the total amount of dust that may condense scale linearly with the metallicity (equation 12).

Old super-metal-rich stars of this kind could populate the nuclear regions of passively evolved elliptical galaxies (Bertola et al. 1995) and it is interesting to notice that at a typical age of 10 Gyr, the turn-off mass is slightly larger than $M = 1.1\,M_{\odot}$ (see Table 1). These stars can reach high dust mass-loss rates of silicate type, and could thus be responsible for the 9.7 μm silicate features discovered with *Spitzer* in the nuclear regions of nearby elliptical galaxies (Bressan et al. 2006). The observed MIR spectral features are quite broad and could be consistent with a size distribution peaked towards large grains, as that shown in Figs 8 and 9.

The lower two panels in Figs 8 and 9 show the dust-to-gas ratios δ, and the condensation fractions f, respectively. Typical values of the silicate dust-to-gas ratios predicted in our models of solar metallicity were around $\delta \sim 1/200$–$1/300$ while at $Z = 0.04$ and $Z = 0.06$ we obtain $\delta \leq 1/200$ and $\delta \leq 1/100$, respectively. A typical value for the dust-to-gas ratio adopted for Galactic M-stars is $\delta \sim 1/200$ (Groenewegen & de Jong 1998), and it is usually scaled linearly with the initial metallicity. At solar metallicity, our predictions agree fairly well with the assumed dust-to-gas ratio. On the other hand, at super-solar metallicities, the dust-to-gas ratios predicted by our models do not increase linearly with the metallicity. This can be seen also by noticing that the condensation fractions, plotted in the lowest panels of the figures, decrease at increasing metallicity. Taking the $M = 1\,M_{\odot}$ model for comparison, we notice that the condensation fraction of olivine decreases from $f_{\rm ol} \sim 0.45$–0.55 at $Z = 0.02$ to $f_{\rm ol} \sim 0.30$–0.40 at $Z = 0.04$ and to $f_{\rm ol} \sim 0.20$–0.40 at $Z = 0.06$. A similar decrease at increasing Z is shown for the condensation fraction of the pyroxene. This effect is likely due to the larger outflow velocity, at a given mass-loss rate, obtained in the more metal-rich envelopes, as a consequence of a larger dust opacity.

6 DUST EJECTA

The integrated ejecta of the main condensed compounds, i.e. silicates, amorphous carbon, iron and SiC, along the entire TP-AGB phase for the different masses and metallicities, are plotted in Fig. 10 and are provided in Table 1. They refer to individual stars and they may not be representative of the corresponding dust ejecta obtained after convolving with the initial mass function. We remind that the integration is performed irrespective of the ability of dust to drive or not the stellar wind, but this unfavourable case occurs in just few models at super-solar metallicity, corresponding to low mass-loss rates. For comparison, we plot in the same figure also the results of Nanni et al. (2013) for the metallicity $Z = 0.02$. At a given mass, the dust ejecta increase with the metallicity, albeit not linearly but $\propto Z^{0.7}$, on average. The silicate ejecta at a given metallicity increase with the mass, but tend to saturate at high masses or even decrease for the case of $M = 5\,M_{\odot}$ at $Z = 0.04$. In the latter case the decrease is due to a C/O ratio that reaches unity towards the end of the evolution (see Fig. 8).

At $Z = 0.04$, we can compare our results with the ones obtained by Zhukovska et al. (2008). Below $M = 3\,M_{\odot}$ and above $M = 4\,M_{\odot}$,
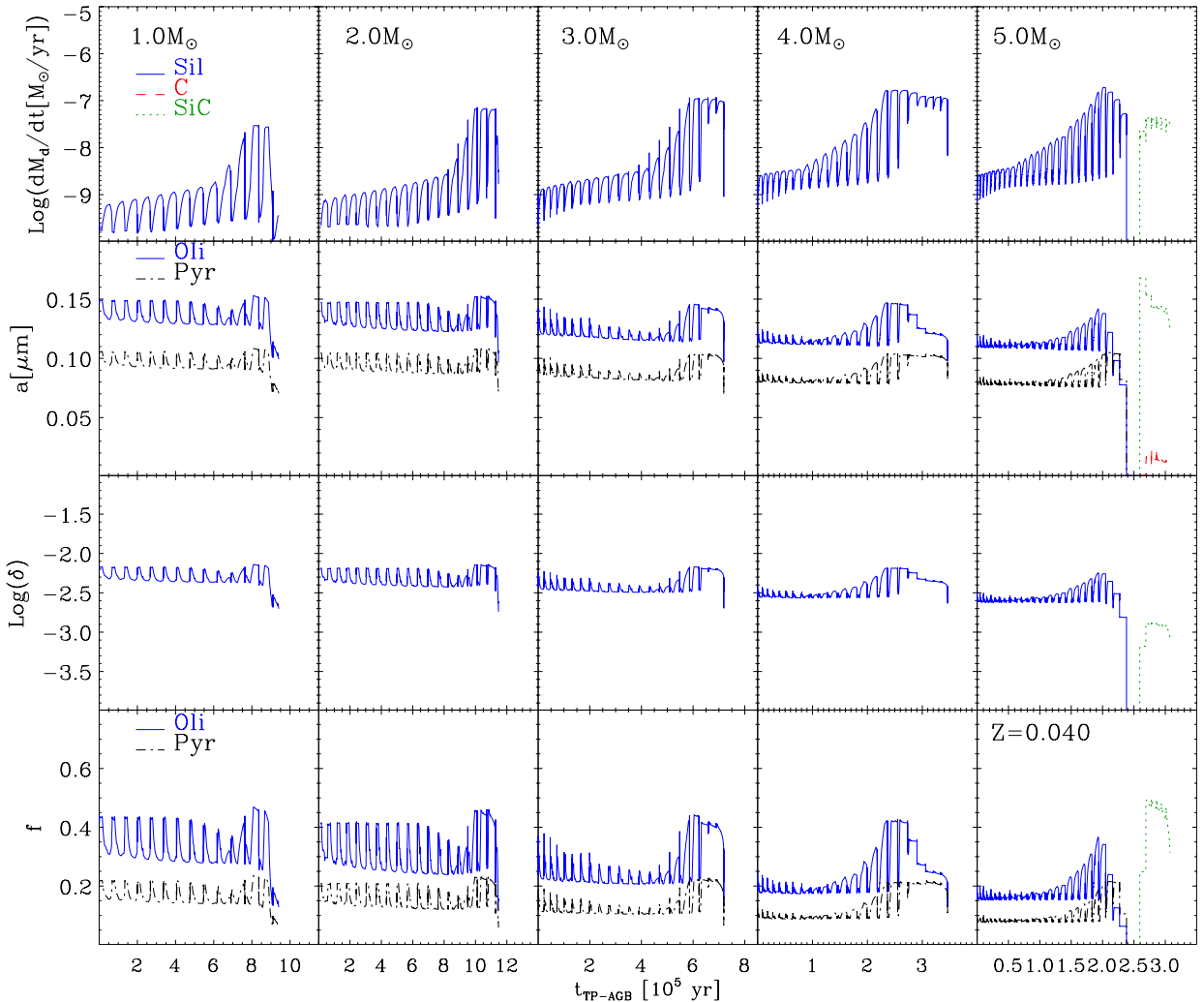
Figure 8. Dust properties of selected models of initial metallicity $Z = 0.04$, for various initial masses, as shown in the upper panels. From top to bottom we depict the dust mass-loss rates in $M_\odot$ yr^{-1}, the dust sizes in μm, the dust-to-gas ratios δ, and the dust condensation fractions f, respectively. The main dust species are silicates (blue lines). For $M = 5\,M_\odot$ amorphous carbon (red lines) and SiC (green lines) are also produced. In some panels silicates are separated into olivine-type dust (blue lines) and pyroxene-type dust (black lines) as indicated in the insets.

the resulting dust ejecta are very similar. On the contrary, in the range between $M = 3$ and $4\,M_\odot$, the dust production in Zhukovska et al. (2008) is dominated by SiC or by amorphous carbon, rather than by silicates as in our models. Furthermore, the iron dust ejecta predicted by Zhukovska et al. (2008) are always higher than those predicted by our models and, in some cases they are comparable to the silicate ones, as for $M = 2.5\,M_\odot$, or to the ones of carbon-bearing dust species, as in the case of $M = 3\,M_\odot$. These differences could be due to effects of neglecting chemisputtering in our models that, anticipating the condensation of silicates, inhibits the production of iron. With the new models presented here, we can draw a consistent picture of how dust production evolves over a wide range of metallicities and for a large mass spectrum. Particularly useful are the ratios between the total dust ejecta and the gas ejecta, which, after being convolved with the stellar initial mass function and the star formation rate, outline the theoretical picture of galactic dust evolution (Dwek et al. 2007; Valiante et al. 2009; Dwek & Cherchneff 2011). Often, in such models the dust-to-mass ratio is scaled with the metallicity, i.e. $\delta(Z)/\delta_\odot = Z/Z_\odot$, skipping all the details of the dust production processes. For $\delta_\odot$ there are different assumptions in literature, but a suitable average is $\delta_\odot = 1/200$. A

value $\delta_\odot = Z_\odot$ is sometimes assumed as an extreme case, if all the metals are supposed to be looked into dust.

In Fig. 11 we compare the predictions of the integrated dust-to-gas ratios, i.e. the ratios between the total dust and gas ejecta M_d/M_g after integration along the AGB track, for several masses and as a function of the metallicity. For the solar and sub-solar metallicities, $Z = 0.001, 0.008, 0.02$, we compute the total dust-to-gas ratio from the models presented in Nanni et al. (2013). We show separately the sum of the silicates and iron ejecta and the sum of these ejecta plus the carbon and SiC ejecta (the global ejecta), all normalized to the gas ejecta. This codification allows one to recognize at once the total dust contribution and the main dust species. Our global ejecta were also compared with the ones obtained by Zhukovska et al. (2008); based on Ferrarotti & Gail (2006) at $Z = 0.001, 0.008, 0.02, 0.04$. In the same figure, the solid line represents the extreme case $\delta_\odot = Z_\odot$ while, the dotted line represents the standard assumption $\delta_\odot = 1/200$.

A striking feature of this figure is that our global dust-to-gas ejecta are much less dependent on the metallicity than that usually assumed. There is of course a modulation with the initial mass but, considering for example $M = 1.5, 2, 3\,M_\odot$, we see that the
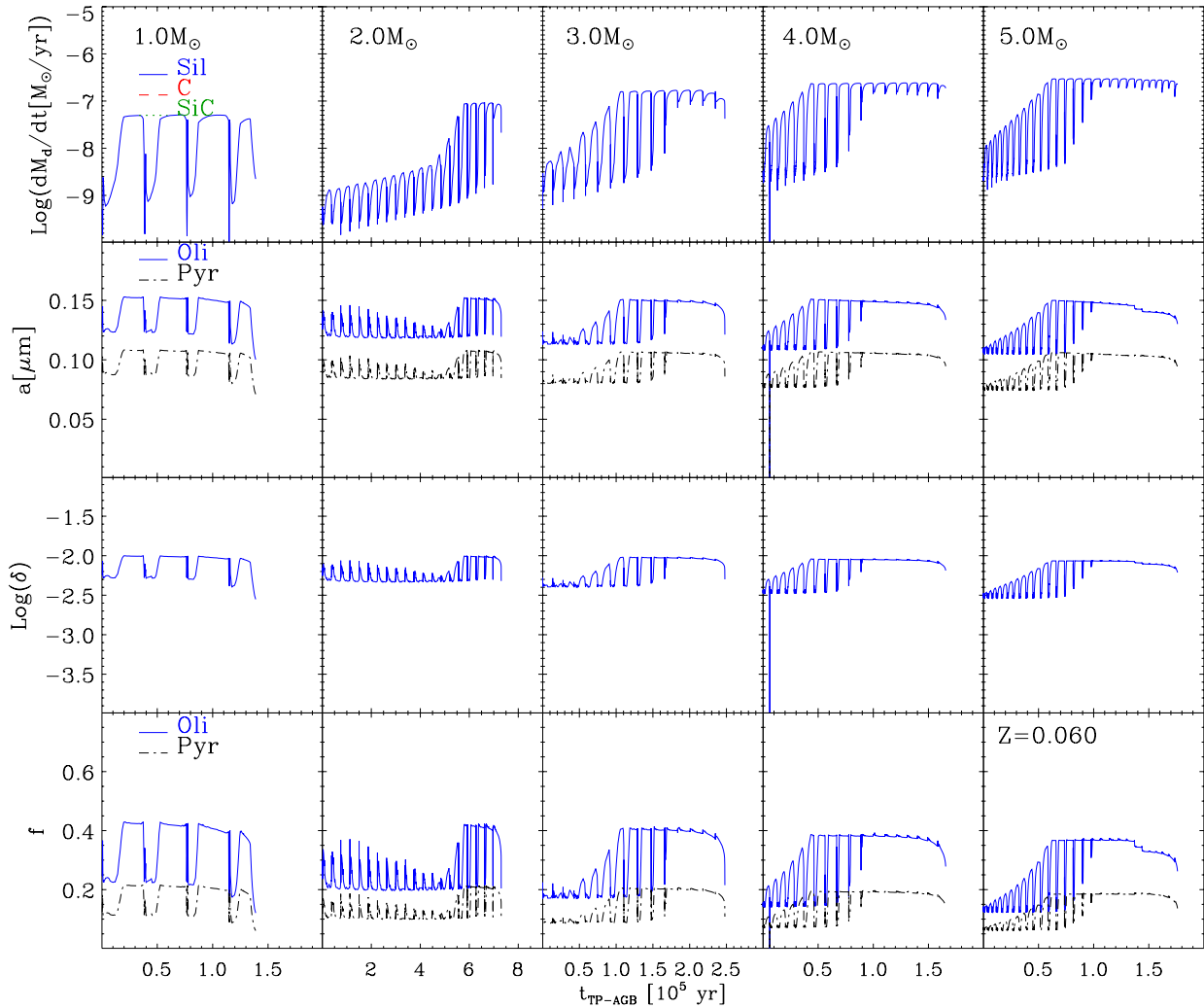
Figure 9. The same as in Fig. 8, but for initial metallicity $Z = 0.06$.
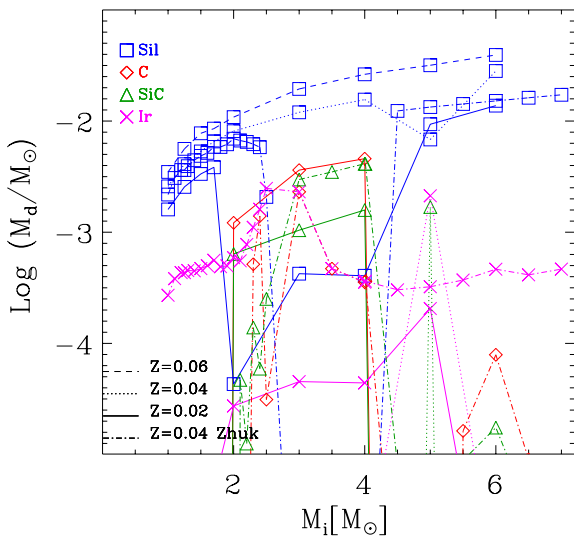

Figure 10. Total dust ejecta as a function of the initial stellar mass and for different initial metallicity, $Z = 0.06$ (dashed lines), $Z = 0.04$ (dotted lines) and, for comparison, $Z = 0.02$ from Nanni et al. (2013) (solid lines). For the case with $Z = 0.04$ we compare our results with the models by Zhukovska et al. (2008) (dot–dashed lines.)
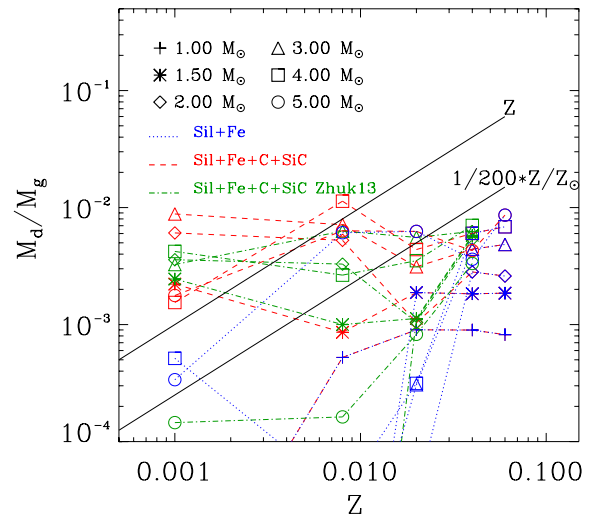
Figure 11. Ratios of dust-to-gas ejecta as a function of the initial stellar mass and initial metallicity. Our results are compared with the ones obtained by Zhukovska et al. (2008), based on Ferrarotti & Gail (2006) (Zhukovska, private communication).

ratios M_d/M_g at super-solar metallicity after an initial decrease at decreasing metallicity, they rise again due to the overproduction of carbon at lower metallicity. In the models presented by Zhukovska et al. (2008), a similar trend is found at $M = 1.5, 2, 4 \, M_\odot$, while, at $M = 3 \, M_\odot$, the dust-to-gas is almost constant in the metallicity range considered. Our models of $M = 1, 4, 5 \, M_\odot$ show a similar behaviour down to $Z = 0.008$ and thereafter they show a decline. In any case the latter models ($M = 4, 5 \, M_\odot$) at the lowest metallicity have ratios that are equal or even slightly larger than the extreme ratio $\delta_\odot = Z_\odot$. On the other hand, the dust-to-gas ratios computed by Zhukovska et al. (2008) show a decline for $M = 1 \, M_\odot$ and $5 \, M_\odot$ below $Z = 0.02$ and, for this latter mass the total dust-to-gas ratio is well below the one predicted by our models. In summary we can say that, at the lowest metallicity the global dust-to-gas ejecta may reach and even encompass the extreme ratio by even an order of magnitude, due to the efficient carbon dust production while, at the highest metallicities, the ratios saturate, possibly due to the abrupt decrease in density produced by the large accelerations of the dusty-driven winds. This behaviour is similar to the one of the models by Zhukovska et al. (2008).

7 SUMMARY AND CONCLUDING REMARKS

In this study we perform the analysis of the formation, evolution and mineralogy of the dust grains expected to form in the outflows of TP-AGB stars with super-solar metallicity, i.e. $Z = 0.04$ and $Z = 0.06$. We apply the dust growth formalism presented in Nanni et al. (2013), which is a modification of the one developed by FG06, to the new TP-AGB evolutionary tracks of high metallicity ($Z = 0.04$, $Z = 0.06$) computed by Marigo et al. (2013).

Nanni et al. (2013) showed that, in order to reproduce the observed relation between velocities and mass-loss rates of Galactic M-giant, one has to inhibit chemisputtering by H_2 molecules, which was instead considered at its full efficiency by FG06 and GS99. Neglecting this dust destruction process is also in agreement with recent experimental results of dust evaporation and condensation. We thus have considered in our formalism only destruction by sublimation. However, at the high metallicities considered here, we find it necessary to take into account also the coupling between dust and gas particles, through a collisions heating rate because dust may form in regions where the temperature and density are so high that collisions can significantly affect the dust equilibrium temperature. We check that this effect is not so important in the case of solar and sub-solar metallicities.

At the high metallicities considered in this work, $Z = 0.04$ and $Z = 0.06$, the third dredge-up is inefficient and the TP-AGB lifetimes are short enough to prevent the formation of carbon stars in most the models here considered. This is consistent with the extremely low ratio of C- to M-giants recently found in M31 (Boyer et al. 2013). The surface C/O ratio remains below unity during the whole TP-AGB evolution of all stellar models, but for the last TP-AGB stages of one massive TP-AGB track. As a consequence, the dust mineralogy is completely dominated by silicates, characteristic of M-type stars. On the other hand, the models by Zhukovska et al. (2008) predict that, at $Z = 0.04$, carbon stars are formed between $M = 2.1 \, M_\odot$ and $4.5 \, M_\odot$ and also around $M = 6 \, M_\odot$. However, in their models dust production is dominated by carbon-bearing species only between $3 \, M_\odot$ and $4 \, M_\odot$.

At super-solar metallicities the expansion velocities are larger than those predicted by models of solar metallicity. We notice that some of the Galactic M-giants with the largest velocities at a given

mass-loss rate could be consistent with super-metal-rich stars with $Z = 0.04$.

In our models, at a given mass, the dust-to-gas ratios increase with the metallicity, but with a dependence which is less than linear, likely due to the feedback produced on the CSE (especially the density) by the large acceleration. This is also shown by the condensation fractions that, at a given mass, decrease with increasing metallicity. A similar trend is also predicted by the models by Zhukovska et al. (2008).

For both metallicities $Z = 0.04, 0.06$, we present the corresponding dust ejecta, which are mainly under the form of silicates. Finally, by combining them with the total mass lost by the star during the AGB phase we obtain the total dust-to-gas ejecta ratios. Adding these results to those obtained by Nanni et al. (2013), for the lower metallicities, $Z = 0.001, 0.008, 0.02$, the following striking global picture emerges. The total dust-to-gas ejecta of intermediate-mass stars are much less dependent on the metallicity than that usually assumed. At the lowest metallicity the total dust-to-gas ejecta may reach and even encompass the value of the corresponding initial metallicity by even an order of magnitude, due to the efficient carbon dust production. At the highest metallicities, the ratios saturate, possibly due to the abrupt decrease in density produced by the large accelerations of the dusty driven winds. While we do think that the picture at the high metallicities is plausible, we warn the reader that the issue of the large carbon dust production at the lowest metallicities is still open and awaits direct observational confirmations (van Loon et al. 2008).

REFERENCES

Barin I., Platzki G., 1995, Thermochemical Data of Pure Substances. No. v. 1 in Thermochemical Data of Pure Substances. VCH
Beelen A., Cox P., Benford D. J., Dowell C. D., Kovács A., Bertoldi F., Omont A., Carilli C. L., 2006, ApJ, 642, 694
Begemann B., Dorschner J., Henning T., Mutschke H., Guertler J., Koempe C., Nass R., 1997, ApJ, 476, 199
Bell K. R., Lin D. N. C., 1994, ApJ, 427, 987
Bertola F., Bressan A., Burstein D., Buson L. M., Chiosi C., di Serego Alighieri S., 1995, ApJ, 438, 680
Bertoldi F. et al., 2003, A&A, 409, L47
Bladh S., Höfner S., Nowotny W., Aringer B., Eriksson K., 2013, A&A, 553, A20
Boyer M. L. et al., 2013, ApJ, 774, 83
Bressan A., Granato G. L., Silva L., 1998, A&A, 332, 135
Bressan A. et al., 2006, ApJ, 639, L55
Bressan A., Marigo P., Girardi L., Salasnich B., Dal Cero C., Rubele S., Nanni A., 2012, MNRAS, 427, 127
Cherchneff I., Barker J. R., Tielens A. G. G. M., 1992, ApJ, 401, 269
Clemens M. S., Bressan A., Panuzzo P., Rampazzo R., Silva L., Buson L., Granato G. L., 2009, MNRAS, 392, 982
Clemens M. S., Panuzzo P., Rampazzo R., Vega O., Bressan A., 2011, MNRAS, 412, 2063
Di Criscienzo M. et al., 2013, MNRAS, 433, 313
Duschl W. J., Gail H.-P., Tscharnuter W. M., 1996, A&A, 312, 624

Dwek E., Cherchneff I., 2011, ApJ, 727, 63

Dwek E., Galliano F., Jones A. P., 2007, Nuovo Cimento B Serie, 122, 959

Eales S., Lilly S., Webb T., Dunne L., Gear W., Clements D., Yun M., 2000, AJ, 120, 2244

Ferrarotti A. S., Gail H.-P., 2006, A&A, 447, 553 (FG06)

Gail H.-P., Sedlmayr E., 1986, A&A, 166, 225

Gail H.-P., Sedlmayr E., 1998, Faraday Discussions, 109, 303

Gail H.-P., Sedlmayr E., 1999, A&A, 347, 594 (GS99)

Gall C., Andersen A. C., Hjorth J., 2011, A&A, 528, A14

González Delgado D., Olofsson H., Kerschbaum F., Schöier F. L., Lindqvist M., Groenewegen M. A. T., 2003, A&A, 411, 123

Goumans T. P. M., Bromley S. T., 2012, MNRAS, 420, 3344

Groenewegen M. A. T., de Jong T., 1998, A&A, 337, 797

Groenewegen M. A. T., Whitelock P. A., Smith C. H., Kerschbaum F., 1998, MNRAS, 293, 18

Hanner M., 1988, Technical Report, Grain Optical Properties

Höfner S., 2008, Physica Scripta Volume T, 133, 014007

Höfner S., 2009, in Henning T., Grün E., Steinacker J., eds, ASP Conf. Ser. Vol. 414. Cosmic Dust – Near and Far. Astron. Soc. Pac., San Francisco, p. 3

Jeong K. S., Winters J. M., Le Bertre T., Sedlmayr E., 2003, A&A, 407, 191

Kimura H., Mann I., Biesecker D. A., Jessberger E. K., 2002, Icarus, 159, 529

Knapp G. R., 1985, ApJ, 293, 273

Kobayashi H., Watanabe S.-I., Kimura H., Yamamoto T., 2009, Icarus, 201, 395

Kobayashi H., Kimura H., Watanabe S.-I., Yamamoto T., Müller S., 2011, Earth, Planets, Space, 63, 1067

Lambert D. L., Gustafsson B., Eriksson K., Hinkle K. H., 1986, ApJS, 62, 373

Landolt-Börnstein, 1968, in Schäfer K., ed., Zahlenwerte und Funktionen. No. v. 5b in Zahlenwerte und Funktionen. Springer-Verlag, Heidelberg

Leksina I., Penkina N., 1967, Fizik. Metall. Metalloved., 23, 344

Lilly S. J., Eales S. A., Gear W. K. P., Hammer F., Le Fèvre O., Crampton D., Bond J. R., Dunne L., 1999, ApJ, 518, 641

Loup C., Forveille T., Omont A., Paul J. F., 1993, A&AS, 99, 291

Lucy L. B., 1971, ApJ, 163, 95

Lucy L. B., 1976, ApJ, 205, 482

Maiolino R., Schneider R., Oliva E., Bianchi S., Ferrara A., Mannucci F., Pedani M., Roca Sogorb M., 2004, Nature, 431, 533

Marchenko S. V., 2006, in Lamers H. J. G. L. M., Langer N., Nugis T., Annuk K., eds, ASP Conf. Ser. Vol. 353. Stellar Evolution at Low Metallicity: Mass Loss, Explosions, Cosmology. Astron. Soc. Pac., San Francisco, p. 299

Marigo P., 2002, A&A, 387, 507

Marigo P., Aringer B., 2009, A&A, 508, 1539

Marigo P., Girardi L., 2007, A&A, 469, 239

Marigo P., Bressan A., Nanni A., Girardi L., Pumo M. L., 2013, MNRAS, 434, 488

Matsuura M. et al., 2009, MNRAS, 396, 918

Matsuura M., Woods P. M., Owen P. J., 2013, MNRAS, 429, 2527

Mattsson L., 2011, MNRAS, 414, 781

Mayya Y. D., Rosa-Gonzalez D., Santiago-Cortes M., Rodriguez-Merino L. H., Vega O., Torres-Papaqui J. P., Bressan A., Carrasco L., 2013, MNRAS, 436, 2763

Michałowski M. J., Watson D., Hjorth J., 2010, ApJ, 712, 942

Nagahara H., Ozawa K., 1996, Geochim. Cosmochim. Acta, 60, 1445

Nagahara H., Ogawa R., Ozawa K., Tamada S., Tachibana S., Chiba H., 2009, in Henning T., Grün E., Steinacker J., eds, ASP Conf. Ser. Vol. 414. Cosmic Dust – Near and Far. Astron. Soc. Pac., San Francisco, p. 403

Nanni A., Bressan A., Marigo P., Girardi L., 2013, MNRAS, 434, 2390

Ossenkopf V., Henning T., Mathis J. S., 1992, A&A, 261, 567

Pègouriè B., 1988, A&A, 194, 335

Pipino A., Matteucci F., 2011, A&A, 530, A98

Pipino A., Fan X. L., Matteucci F., Calura F., Silva L., Granato G., Maiolino R., 2011, A&A, 525, A61

Robson I., Priddey R. S., Isaak K. G., McMahon R. G., 2004, MNRAS, 351, L29

Råback P., 1999, Modelling of the Sublimation Growth of Silicon Carbide Crystals. CSC Research Reports: Centre for Scientific Computing, Center for Scientific Computing

Schöier F. L., Ramstedt S., Olofsson H., Lindqvist M., Bieging J. H., Marvel K. B., 2013, A&A, 550, A78

Sharp C. M., Huebner W. F., 1990, ApJS, 72, 417

Smith V. V., Lambert D. L., 1985, ApJ, 294, 326

Tielens A. G. G. M., Waters L. B. F. M., Molster F. J., Justtanont K., 1998, Ap&SS, 255, 415

Valiante R., Schneider R., Bianchi S., Andersen A. C., 2009, MNRAS, 397, 1661

Valiante R., Schneider R., Salvadori S., Bianchi S., 2011, MNRAS, 416, 1916

van Loon J. T., Cohen M., Oliveira J. M., Matsuura M., McDonald I., Sloan G. C., Wood P. R., Zijlstra A. A., 2008, A&A, 487, 1055

Vassiliadis E., Wood P. R., 1993, ApJ, 413, 641

Ventura P. et al., 2012, MNRAS, 424, 2345

Woitke P., 2006, A&A, 460, L9

Yamasawa D., Habe A., Kozasa T., Nozawa T., Hirashita H., Umeda H., Nomoto K., 2011, ApJ, 735, 44

Zhukovska S., Henning T., 2013, A&A, 555, A99

Zhukovska S., Gail H.-P., Trieloff M., 2008, A&A, 479, 453

This paper has been typeset from a TEX/LATEX file prepared by the author.